

# Quantum transport properties of monolayer graphene with antidot lattice

Cite as: J. Appl. Phys. **126**, 084305 (2019); <https://doi.org/10.1063/1.5100813>

Submitted: 23 April 2019 . Accepted: 08 August 2019 . Published Online: 23 August 2019

Leizhi Wang , Ming Yin, Bochen Zhong, Jan Jaroszynski, Godwin Mbamalu, and Timir Datta



View Online



Export Citation



CrossMark

## ARTICLES YOU MAY BE INTERESTED IN

[Fluorescence microscopy of biophysical protein dynamics in nanoporous hydrogels](#)

Journal of Applied Physics **126**, 081101 (2019); <https://doi.org/10.1063/1.5110299>

[Antiferromagnetic excitons in graphene nanodots](#)

Journal of Applied Physics **126**, 084307 (2019); <https://doi.org/10.1063/1.5099112>

[Plasmonic visible-NIR photodetector based on hot electrons extracted from nanostructured titanium nitride](#)

Journal of Applied Physics **126**, 083108 (2019); <https://doi.org/10.1063/1.5101009>

## Ultra High Performance SDD Detectors



See all our XRF Solutions

# Quantum transport properties of monolayer graphene with antidot lattice

Cite as: J. Appl. Phys. 126, 084305 (2019); doi: 10.1063/1.5100813

Submitted: 23 April 2019 · Accepted: 8 August 2019 ·

Published Online: 23 August 2019



View Online



Export Citation



CrossMark

Leizhi Wang,<sup>1,2</sup>  Ming Yin,<sup>3</sup> Bochen Zhong,<sup>2</sup> Jan Jaroszynski,<sup>4</sup> Godwin Mbamalu,<sup>3</sup> and Timir Datta<sup>2,a)</sup>

## AFFILIATIONS

<sup>1</sup>Energy Sciences Institute, Yale University West Campus, West Haven, Connecticut 06516, USA

<sup>2</sup>Department of Physics and Astronomy, University of South Carolina, Columbia, South Carolina 29208, USA

<sup>3</sup>Department of Physics and Engineering, Benedict College, Columbia, South Carolina 29204, USA

<sup>4</sup>National High Magnetic Field Laboratory, Tallahassee, Florida 32310, USA

<sup>a)</sup>Author to whom correspondence should be addressed: [datta@mailbox.sc.edu](mailto:datta@mailbox.sc.edu)

## ABSTRACT

Quantum transport properties in monolayer graphene are sensitive to structural modifications. We find that the introduction of a hexagonal lattice of antidots has a wide impact on weak localization and Shubnikov-de Haas (SdH) oscillation of graphene. The antidot lattice reduces both phase coherence and intervalley scattering length. Remarkably, even with softened intervalley scattering, i.e., the phase-breaking time is shorter than intervalley scattering time, coherence between time reversed states remains adequate to retain weak localization, an offbeat and rarely reported occurrence. Whereas SdH oscillation is boosted by the antidot lattice, the amplitude of the SdH signal rises rapidly with the increasing antidot radius. But both effective mass and carrier density are reduced in a larger antidot lattice. A bandgap of  $\sim 10$  meV is opened. The antidot lattice is an effective dopant-free way to manipulate electronic properties in graphene.

Published under license by AIP Publishing. <https://doi.org/10.1063/1.5100813>

## I. INTRODUCTION

Graphene, a single and isolated atomic layer of graphite, was the first truly two-dimensional material to be discovered. Its unorthodox electronic band structure, with linear dispersion relation plus Dirac points, gives rise to an intriguing combination of electron-hole degeneracy, almost-zero effective mass, ultrahigh mobility, and long mean free path.<sup>1–6</sup> Even compared with other carbon systems, the potential for graphene is enthralling.<sup>7,8</sup> Unsurprisingly, graphene is an exceptional platform for testing fundamental physics and many technologically important phenomena such as Shubnikov-de Haas oscillation,<sup>2,3,9,10</sup> weak localization,<sup>11–15</sup> quantum Hall effect,<sup>2,3,5</sup> and spin-orbit interaction.<sup>16</sup> Potentially, these features may make graphene the long sought transformational material for practical devices of the future.

Antidot lattice has attracted great interest since it can effectively tune the electronic properties of graphene. Such regular array of holes impose periodic potential barriers and are able to create a bandgap in graphene.<sup>6,16,17</sup> By tuning the size, shape, and symmetry of both the hole and the lattice cell, the band structure can be modified,<sup>6,17–22</sup> hence resulting in the change of electronic and transport properties of materials. Shubnikov-de Haas oscillation may

display structural dependence since it is closely related to the effective mass due to the Fermi surface. Weak localization might be influenced when the antidot lattice constant is comparable to the phase coherence length. However, a systematic understanding of the relation between electronic properties and antidot geometry in graphene has not yet been attained and more effort is needed.

In this article, magnetotransport has been measured under a magnetic field up to 31 T at different temperatures down to 0.37 K. We report on the structural dependence of weak localization and Shubnikov-de Haas oscillation in monolayer CVD (chemical vapor deposition) graphene with the antidot lattice. Remarkably, weak localization is observed, even though intervalley scattering time is found to be longer than phase-breaking time; this seemingly curious behavior is rare and has only been reported in a few instances.<sup>11,23</sup> When antidots are introduced, phase coherence length and intervalley scattering length become smaller. Temperature dependence of phase scattering time indicates that electron-electron interaction results in phase breaking. Moreover, Shubnikov-de Haas (SdH) oscillation displays size dependence with changing radius of antidot. The amplitude of SdH oscillation is boosted, and its peak shifts toward the lower magnetic field with the increasing hole radius; both carrier

density and effective mass are reduced correspondingly. These observations confirm that the antidot lattice is an effective nonchemical way to manipulate electronic properties of graphene.

## II. EXPERIMENTS

Our single layer graphene on the Si substrate with 300 nm thermal oxide was grown by chemical vapor deposition (CVD) method, with a mobility of  $1008 \text{ cm}^2/(\text{V s})$  at low temperature 2 K. The antidot lattice and device isolation were defined by electron beam lithography (JEOL). The patterns were then etched for 6 s using  $\text{O}_2$  plasma by reactive ion etcher (RIE) with inductively coupled plasma (ICP) and RIE power both at 50 W. A Hall bar with six Ohmic contacts was defined by the second-step electron beam lithography. Ti/Au (8 nm/50 nm) films were deposited on the samples using an electron beam evaporator operating at  $1 \times 10^{-6}$  Torr. The inset of Fig. 1(a) shows a schematic diagram of the Hall bar device, with the channel width of  $\sim 9 \mu\text{m}$ , and the length between the voltage probes of  $\sim 15 \mu\text{m}$ . Electrical and magnetotransport measurements were conducted in 31 T, 50 mm Bore Magnet (Cell 9) with  $^3\text{He}$  insert at the National High Magnetic Field Laboratory (NHMFL). The input current with  $1 \mu\text{A}$  at 17.73 Hz was applied by a lock-in amplifier (SR830 DSP).

## III. RESULTS AND DISCUSSION

### A. Weak localization

Figure 1(a) shows scanning electron microscopy (Zeiss Ultra Plus FESEM) image of the graphene antidot lattice with a hole

radius of  $r = 125 \text{ nm}$ . The antidot lattice is a hexagonal array of circular holes. As the radius is varied between different sets of samples, the nearest edge distance between two antidots is held constant at 200 nm. In our study, we compare  $r = 125 \text{ nm}$ ,  $r = 50 \text{ nm}$ , and  $r = 0 \text{ nm}$  (pristine graphene). Raman spectrum of chemical vapor deposited graphene is displayed in Fig. 1(b). 2D peak at  $2660 \text{ cm}^{-1}$  is much larger than G peak at  $1600 \text{ cm}^{-1}$ , indicating that our graphene is monolayer.<sup>24–26</sup>

Due to the roles of chirality and Berry phase, weak localization of monolayer graphene is very different from that in conventional two-dimensional systems.<sup>27</sup> Because the Berry phase is  $\pi$  in monolayer graphene, the two trajectories are expected to gain a phase difference of  $\pi$ . However, chirality is reversed between the two valleys, and thus zero phase difference between two self-intersecting trajectories is allowed in the presence of significant intervalley scattering. The correction to the change of magnetoconductivity of graphene is given by<sup>11,12,17,28</sup>

$$\Delta\sigma(B) = \frac{e^2}{\pi h} \left[ F\left(\frac{B}{B_\phi}\right) - F\left(\frac{B}{B_\phi + 2B_i}\right) - 2F\left(\frac{B}{B_\phi + B_i + B_*}\right) \right],$$

$$F(z) = \ln z + \psi\left(\frac{1}{2} + \frac{1}{z}\right), \quad B_{\phi,i,*} = \frac{\hbar}{4De} \tau_{\phi,i,*}^{-1}. \quad (1)$$

Here,  $\psi(z)$  is the digamma function,  $\tau_\phi$  is the phase-breaking time,  $\tau_i$  is the elastic intervalley scattering time and  $\tau_*^{-1} = \tau_w^{-1} + \tau_z^{-1}$ , where  $\tau_w$  is related to trigonal warping and  $\tau_z$  is the intravalley

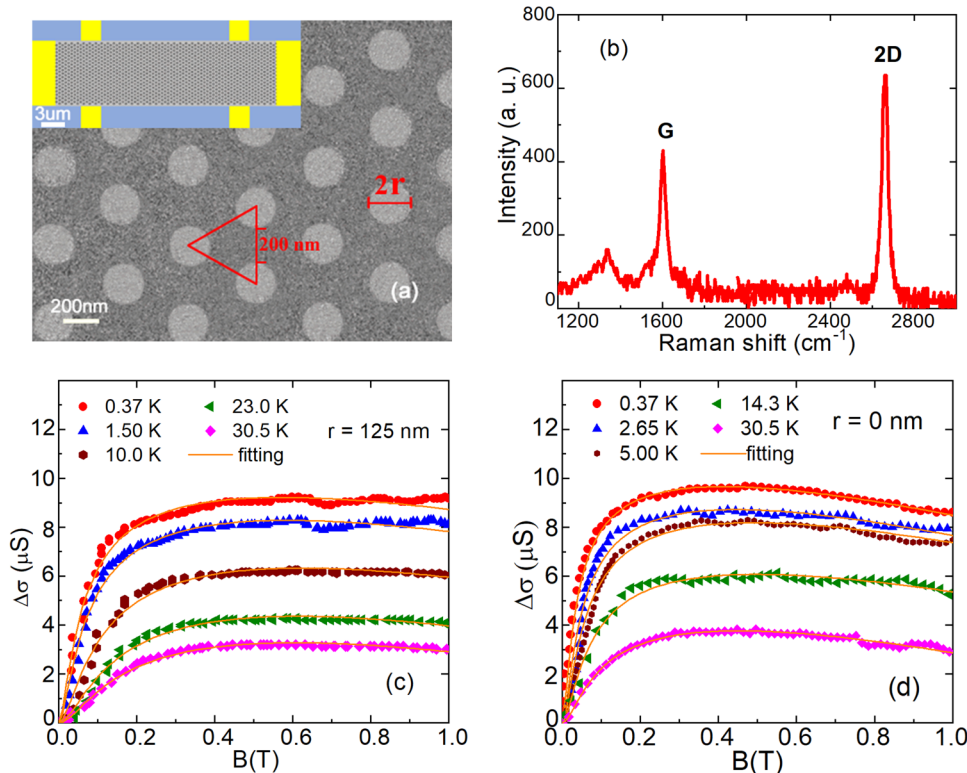


**FIG. 1.** (a) SEM image of the graphene antidot lattice, which is composed of a hexagonal array of circular holes. The radius of antidot is around 125 nm; the nearest edge distance between two antidots is 200 nm. The inset shows a schematic diagram of the Hall bar device. (b) Raman spectrum of CVD monolayer graphene. Magnetoconductivity at a set of temperatures for (c)  $r = 125 \text{ nm}$  antidot lattice and (d) pristine graphene. The yellow curves are the best fitting to Eq. (1).

scattering time; here the contribution of  $\tau_i$  is not included. The corresponding length is  $L_{\phi,i^*} = \sqrt{D\tau_{\phi,i^*}}$ , where  $D$  is the diffusion constant given by  $D = v_F^2\tau_t/2$  and  $\tau_t$  is the transport scattering time obtained from the carrier mobility.

The first term in Eq. (1) is responsible for positive magnetoconductivity, i.e., weak localization, while the second and third terms lead to antilocalization. Hence, when the intervalley and intravalley scattering are strong enough ( $\tau_\phi > \tau_i, \tau^*$ ), the first term dominates, resulting in positive  $\Delta\sigma$  and weak localization. Situations where the phase-breaking time  $\tau_\phi$  is larger than intervalley and intravalley scattering time are common and have been reported by numerous experiments.<sup>11,12,29</sup> For instance, the intervalley scattering in exfoliated monolayer graphene is usually very strong since graphene is tightly coupled to the substrate and weak localization can be easily observed.<sup>14</sup> For our present monolayer graphene and antidot structures, the conductivity curves shown in Figs. 1(c) and 1(d) increase with the increasing magnetic field, and weak localization is also noticed. This effect becomes much stronger at low temperatures. We use Eq. (1) to fit experimental data, and analysis of each term has been shown in Fig. S1 in the supplementary material. From the best fit, we computed the scattering times and lengths for these samples. Interestingly, here the intervalley scattering length  $L_i$  is larger than the phase coherence length  $L_\phi$ , correspondingly  $\tau_i > \tau_\phi$  for both graphene and  $r = 125$  nm antidot samples. Tikhonenko *et al.* have analyzed the condition for weak localization and antilocalization.<sup>11</sup> As shown in Fig. 2(a), the yellow curve separates the regions of localization and antilocalization. We can clearly see that when the phase-breaking time is smaller than the intervalley scattering time  $\tau_\phi < \tau_i$ , weak localization can still be observed if  $\tau_\phi \gg \tau^*$ . Our data fall into this frontier ( $\sim$ top left quarter) regime; consequently, localization ensues, although  $\tau_\phi/\tau_i < 1$ . This means that the intervalley scattering in our graphene is very weak, which might be due to the fact that the graphene layer is relatively loosely coupled to the substrate, thereby effectively reducing the contribution of atomically sharp scatters.<sup>14,23</sup>

Secondly, phase coherence length  $L_\phi$  and intervalley scattering length  $L_i$  are decreased when the antidot is introduced. As we

know, intervalley scattering can be enhanced by atomically sharp defects. The introduction of antidot results in more edges, leading to stronger intervalley scattering in antidot samples. Hence, a smaller  $L_i$  is observed for graphene with the antidot lattice in Fig. 2(b). But the intervalley scattering length is still longer than phase coherence length  $L_\phi$  since  $L_\phi$  is also decreased by the introduction of the antidot.

The temperature dependence of  $\tau_\phi$  contains the inelastic scattering information responsible for phase breaking of charge carriers. As shown in Fig. 2(b), phase coherence length increases when the temperature is decreasing. We did not find the saturation of  $L_\phi$  at low temperatures. The inelastic phase-breaking rate is calculated, and it is linearly proportional to temperature,  $\tau_\phi^{-1} \propto T$  in Fig. 2(c). This linearity has been attributed to phase breaking by inelastic electron-electron scattering.<sup>11,12</sup> In addition, we reason that the introduction of the antidot structures is responsible for the decrease of dephasing time/length. Since dephasing rate  $\tau_\phi^{-1} = ak_B T \frac{\ln(g)}{hg}$ , where  $g(n)$  is the normalized conductivity defined as  $g(n) = \sigma(n)h/e^2$ . Several articles have shown that the sample with a larger carrier density has longer phase coherence length.<sup>29-31</sup> Our pristine graphene has a larger carrier density than that of the antidot sample. The introduction of the antidot lattice results in a lower carrier density and shorter coherence length.

## B. Shubnikov-de Haas oscillation

The magnetoresistance for the graphene antidot lattice with hole radius  $r = 125$  nm at a magnetic field of up to 31 T is shown in Fig. 3(a), where the magnetic field is applied perpendicular to the film. Above 7 T, Shubnikov-de Haas oscillations appear and become prominent at larger fields. To clearly highlight these oscillations, the background resistance has been subtracted out, and the residual  $\Delta R$  is shown as a function of  $1/B$  in Fig. 3(b). Here, the background is determined by averaging the curves connecting the maxima and minima, respectively. Obviously, these oscillations exhibit temperature dependence, and their amplitudes are reduced with the increasing temperature.

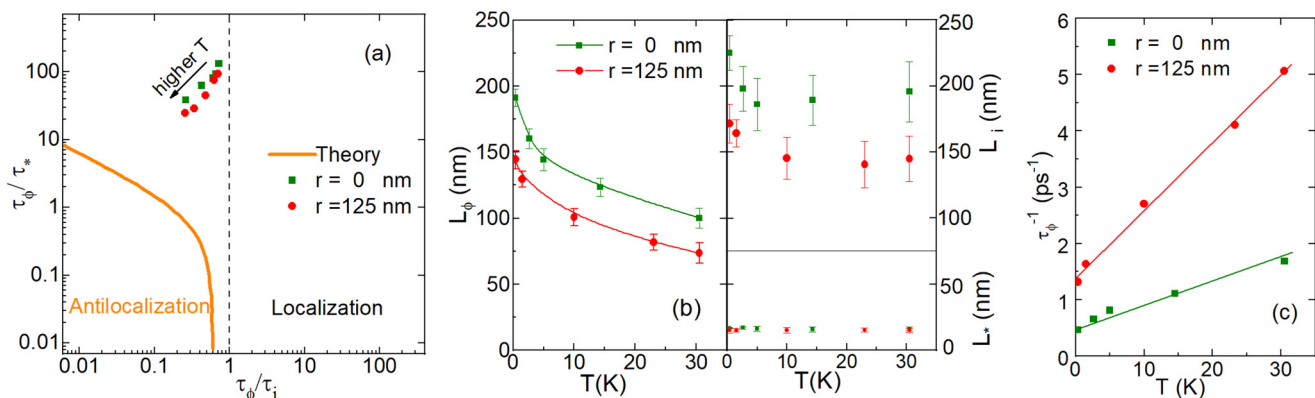


**FIG. 2.** Weak localization effect for  $r = 125$  nm antidot lattice and pristine graphene. (a) A diagram of the scattering times, the yellow curve separates localization and antilocalization regions.<sup>11</sup> (b) Temperature dependence of scattering lengths. (c) Phase-breaking rate as a function of temperature.

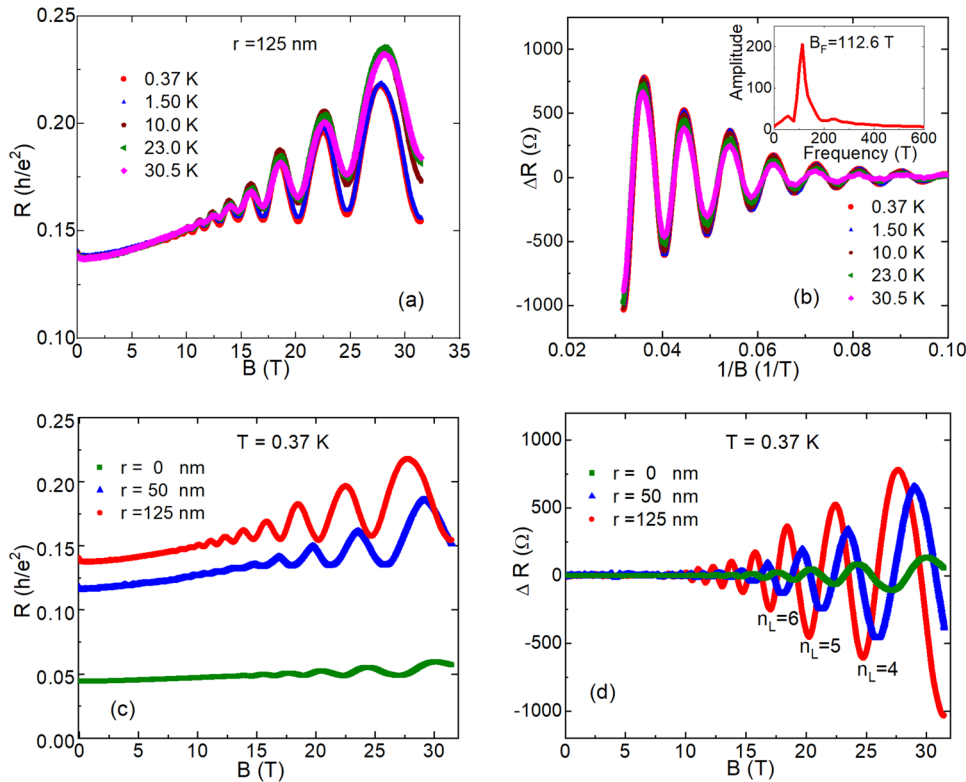


**FIG. 3** (a) Magnetoresistance as a function of the magnetic field at a set of temperatures for monolayer graphene with  $r = 125$  nm antidot lattice, pronounced Shubnikov-de Haas (SdH) oscillations are observed. (b) SdH as a function of  $1/B$  after subtracting the background. Fourier transform analysis is shown in the inset. (c) Magnetoresistance of monolayer graphene with the antidot lattice at 0.37 K, antidot radius is defined as 0 nm (pristine graphene), 50 nm, and 125 nm. (d) Comparison of SdH oscillations after subtracting the background.

Shubnikov-de Haas oscillation can be expressed as<sup>2,32,33</sup>  $\Delta R \propto \frac{\chi}{\sinh(\chi)} \exp\left(\frac{-\pi}{\omega_c \tau_q}\right)$ , where  $\chi = 2\pi^2 k_B T / \Delta E$ ,  $\Delta E = \hbar \omega_c = \hbar e B / m^*$ ,  $k_B$  is the Boltzmann constant,  $\hbar$  is the reduced Planck constant,  $e$  is the electron charge, and  $\tau_q$  is the quantum lifetime. In fact, the SdH oscillation is a periodic function of  $1/B$ , and the oscillation frequency  $B_F$  in Tesla corresponds to the magnetic field of  $n_L = 0$  Landau level. We obtained frequency  $B_F = 112.6$  T from fast Fourier transform (FFT) analysis as shown in the inset of Fig. 3(b). Furthermore, the carrier density has the following relation with oscillation frequency  $n_{SdH} = 4eB_F/h$ ; here the factor of 4 accounts for the fourfold degeneracy due to double spin and double valley in graphene.<sup>3</sup> For the  $r = 125$  nm graphene sample, the carrier density is calculated to be  $n_{SdH} = 1.067 \times 10^{13} \text{ cm}^{-2}$ .

In order to study the size effect of antidot, graphene antidot lattices with different radii were measured. Three effects are observed in Fig. 3(c). First, the resistance is increased. The introduction of the antidot lattice brings in more scatterings, hence leading to larger resistance in antidot samples than that of pristine graphene. Second, the magnitude of oscillations is enhanced by the antidot lattice. When the lattice is introduced and its radius is increased, the SdH signal becomes prominent as shown in Fig. 3(d). The peak value is almost  $800 \Omega$  for the  $r = 125$  nm sample at around 28 T, whereas it is only  $136 \Omega$  at 30 T for pristine graphene. Table I lists several parameter values associated with the  $n_L = 4$  Landau level. Clearly, the SdH oscillation is boosted with the increasing antidot radius. Lastly, the corresponding magnetic

field of peaks or valleys also displays geometry dependence, it moves to the lower field with the increasing hole size. For the same Landau level, such as  $n_L = 4$ , the magnetic field is 27.2 T, 25.9 T, and 24.7 T for  $r = 0$  nm, 50 nm, and 125 nm samples, respectively. From the Fourier transform analysis, the oscillation frequency  $B_F$  is obtained and listed in Table I. The sample with larger hole radius has a smaller  $B_F$ , which corresponds to a smaller carrier density. In other words, the carrier density decreases with the increasing hole radius. Based on the above observations, we conclude that the antidot size indeed affects the properties of graphene.

The inverse relation of the carrier density with antidot radius is also shown by the Landau fan diagram in Fig. 4(a). The intercept in the Landau index is the associated Berry phase  $\beta$ .<sup>2,3,9</sup> Through linear regression of the data, we find  $\beta \sim 0.5$  for all three samples, hence, Berry phase  $\varphi_B = 2\pi\beta \cong \pi$ , indicating the presence of the Dirac fermion.<sup>3,9,34</sup> However, the slope from the fitting for each

**TABLE I.** Comparison of electronic properties of the graphene antidot lattice with different radii.

Antidot radius	$ \Delta R $ ( $\Omega$ ) for $n_L = 4$	$B_F$ (T)	$n_{SdH}$ ( $\text{cm}^{-2}$ )	$\mu$ [ $\text{cm}^2/(\text{V s})$ ]	$m^*$
$r = 0$ nm	110	126.7	$1.225 \times 10^{13}$	1008	$0.087m_e$
$r = 50$ nm	461	114.6	$1.108 \times 10^{13}$	423	$0.078m_e$
$r = 125$ nm	607	112.6	$1.067 \times 10^{13}$	368	$0.064m_e$

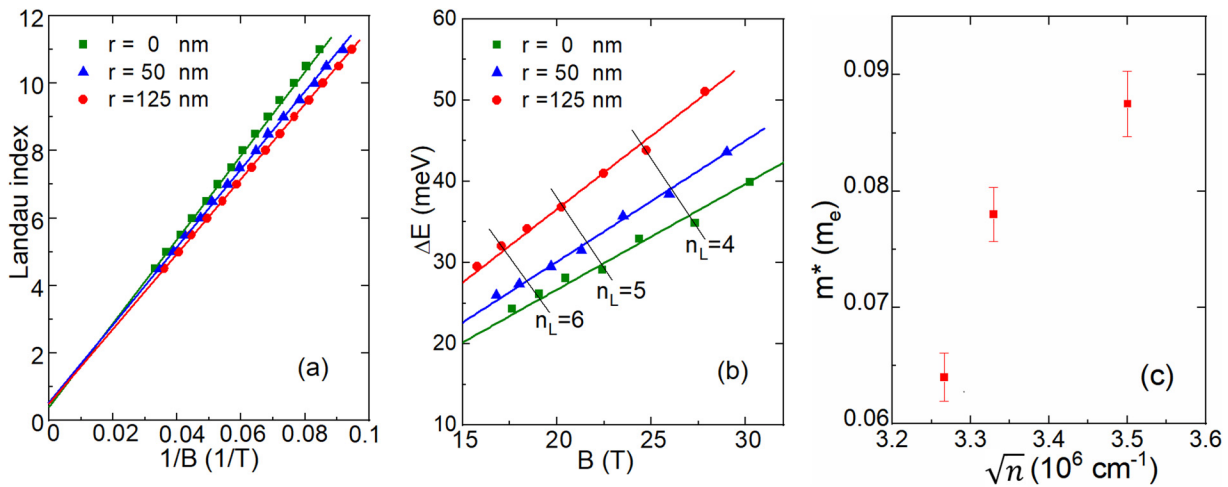


FIG. 4. (a) The Landau fan diagram, the intercept in the Landau index is the associated Berry phase  $\beta$ . (b) Field dependence of Landau level spacing. (c) Effective mass and carrier density relation.

sample is different, where the slope means the SdH oscillation frequency  $B_F$ . Pristine graphene is observed to have the largest slope and  $B_F$ , hence the largest carrier density according to  $n_{sDH} = 4eB_F/h$ . As a result, with the increasing hole radius, slope becomes smaller and the carrier density is reduced correspondingly. Note that the carrier density obtained by the Landau fan diagram and Fourier transform remains the same.

The effective mass  $m^*$  of carrier also displays geometric dependence, and it decreases with the increasing antidot radius.  $m^*$  can be extracted from the temperature dependence of the SdH amplitude at a constant magnetic field by  $\frac{\Delta R(T, B)}{\Delta R(T_0, B)} = \frac{T \sinh(2\pi^2 k_B T_0 / \Delta E(B))}{T_0 \sinh(2\pi^2 k_B T / \Delta E(B))}$ . Here, we choose the lowest temperature 370 mK as  $T_0$ . The Landau level spacing  $\Delta E(B) = \hbar e B / m^*$  from the best fitting for different magnetic fields is shown in Fig. 4(b). The effective mass  $m^*$  can be obtained from the slope of the linear fitting, and there is an inverse relation between the effective mass and slope. For all three samples, pristine graphene has the smallest slope, and the slope increases with the

increasing antidot radius. Using the slope, the effective mass is calculated to be  $0.087m_e$ ,  $0.078m_e$ ,  $0.064m_e$ , respectively, for samples with hole radius  $r=0$  nm, 50 nm, and 125 nm ( $m_e$  is the mass of a free electron). As indicated by experimental data, the effective mass decreases with the increasing hole size. It is worth noting that the carrier density and effective mass have similar relation with antidot radius.<sup>35</sup> Since the effective mass is increased with the increasing carrier density,  $m^* = \frac{E_F}{v_F} = \frac{\hbar k_F}{v_F} = \frac{\hbar \sqrt{\pi} \sqrt{n}}{v_F}$ , here  $k_F^2/\pi = n$ ,  $k_F$  is the Fermi wave vector.<sup>2,3,36</sup> If pristine graphene has the largest carrier density, the effective mass is consequently largest. This is consistent with our experimental data, and the carrier density and effective mass both decrease with the increasing antidot size. Figure 4(c) shows the relation between square root of the carrier density and effective mass. The Fermi velocity is calculated to be  $0.83 \times 10^6$  m/s,  $0.869 \times 10^6$  m/s, and  $1.046 \times 10^6$  m/s for  $r=0$  nm, 50 nm, 125 nm antidot lattice samples, respectively. The difference of the Fermi velocity might indicate the change of band dispersion.

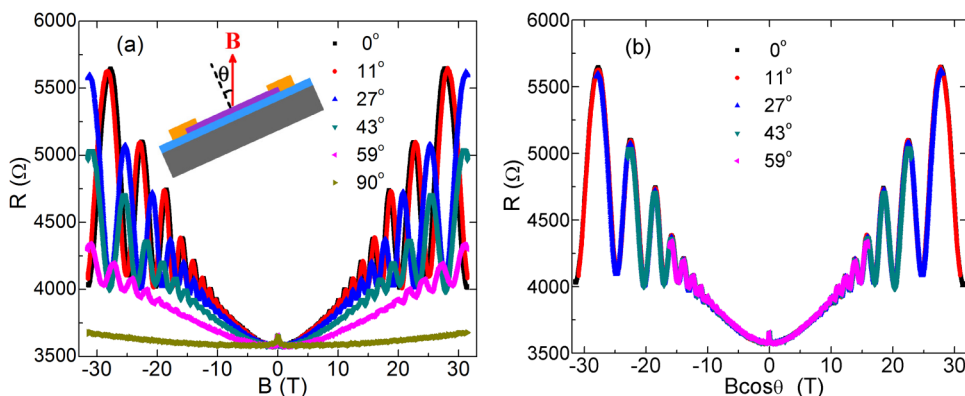


FIG. 5 (a) Angle dependence of magnetoresistance for the graphene antidot lattice at  $T=0.37$  K. The radius of antidot is 125 nm. The inset shows the schematic diagram of the angle definition. (b) Rescale magnetoresistance as a function of  $B \cos \theta$ . All data at different angles collapse into a single curve.

### C. The relative orientation dependence

The angle dependence of magnetoresistance has also been investigated to show the two-dimensional nature of carriers in the graphene antidot lattice. We define  $\theta$  as the angle between the direction of the magnetic field and the normal direction of the graphene plane, as shown in the schematic diagram of Fig. 5(a). Magnetoresistance for the  $r = 125$  nm sample at 370 mK has been measured at angles from  $0^\circ$  to  $90^\circ$ . At  $\theta = 0^\circ$ , when the magnetic field is perpendicular to the sample, the SdH oscillation is pronounced. When the angle is increased, the amplitude of the SdH oscillation becomes smaller. The peaks of the oscillations shift toward the higher magnetic field. At  $\theta = 90^\circ$ , where the magnetic field is parallel to graphene surface and along the current configuration, no oscillation is observed and resistance changes slowly with the magnetic field. We have plotted the magnetoresistance as a function of perpendicular component of the magnetic field,  $B \cos \theta$ . Peaks at different angles in Fig. 5(b) collapse together, showing a universal curve. Hence, the behavior of carriers in graphene exhibits its two-dimensional nature.<sup>27,32</sup>

### D. Bandgap

Temperature dependence of resistance for three samples has been measured and shown in Fig. S2 in [supplementary material](#). Pristine graphene generally exhibits temperature insensitivity. However, the resistance in the antidot lattice sample increases with the decreasing temperature. The activation bandgap is estimated by the following equation,  $R = R_0 \exp(E_a/2k_B T)$ , where  $E_a$  is the activation energy and  $R_0$  is a constant. Figure 6 shows the Arrhenius plot for two samples. The bandgap is calculated to be 10.4 meV for the  $r = 50$  nm antidot lattice and 7.9 meV for the  $r = 125$  nm sample at high temperature. Generally, the induced bandgap in

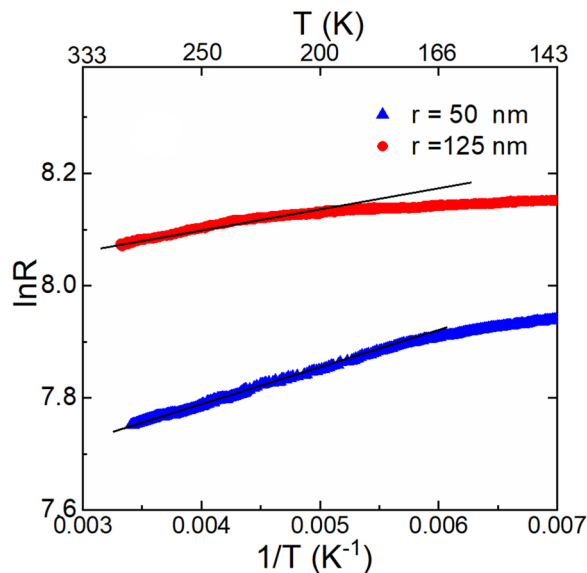


FIG. 6 The Arrhenius plot to extract the activation gap.

the graphene antidot lattice is inversely proportional to the lattice constant and neck width.<sup>6,22,37</sup> Eroms *et al.*<sup>17</sup> reported a bandgap around 6 meV with similar antidot dimension. Jessen *et al.*<sup>38</sup> have reported graphene superlattice encapsulated by hexagonal boron nitride (hBN), and they found a very large energy gap  $\sim 148$  meV in a lattice with a period of 35 nm and a minimum feature size of 13 nm. With the protection of hBN during fabrication, high mobility and true bandgap can be realized.

### IV. CONCLUSIONS

The introduction of the antidot lattice has great influence on transport properties of graphene. We observe that the antidot lattice reduces the phase coherence length and intervalley scattering length. Although weak localization is easily observed when phase-breaking time is longer than intervalley scattering time, we find that coherence remains adequate to retain weak localization even if the phase-breaking time in our graphene is shorter than the intervalley scattering time. In addition, Shubnikov-de Haas oscillations are extremely sensitive to the hole size. With the increasing antidot radius, the amplitude of Shubnikov-de Haas oscillation is enhanced. Moreover, the carrier density, mobility, and effective mass are reduced with the increasing hole size. The introduction of the antidot lattice opens a  $\sim 10$  meV bandgap. Therefore, quantum transport and electronic properties in graphene can be effectively tuned by the antidot lattice.

### SUPPLEMENTARY MATERIAL

See the [supplementary material](#) for details on weak localization fitting, each term contribution, and temperature dependent resistance.

### ACKNOWLEDGMENTS

One of us, T.D., would like to dedicate this work to Mildred Dresselhaus. The work is supported, in part, by the U.S. Department of Energy (DOE) under Award No. DE-NA0002630 and the University of South Carolina. A portion of this work was performed at the National High Magnetic Field Laboratory, which is supported by the National Science Foundation (NSF) under Cooperative Agreement No. DMR-1157490 and the State of Florida.

### REFERENCES

- Y. Zhang, T.-T. Tang, C. Girit, Z. Hao, M. C. Martin, A. Zettl, M. F. Crommie, Y. R. Shen, and F. Wang, *Nature* **459**, 820 (2009).
- Y. Zhang, Y.-W. Tan, H. L. Stormer, and P. Kim, *Nature* **438**, 201 (2005).
- K. S. Novoselov, A. K. Geim, S. V. Morozov, D. Jiang, M. I. Katsnelson, I. V. Grigorieva, S. V. Dubonos, and A. A. Firsov, *Nature* **438**, 197 (2005).
- A. K. Geim and K. S. Novoselov, *Nat. Mater.* **6**, 183 (2007).
- A. Sandner, T. Preis, C. Schell, P. Giudici, K. Watanabe, T. Taniguchi, D. Weiss, and J. Eroms, *Nano Lett.* **15**, 8402 (2015).
- F. Ouyang, S. Peng, Z. Liu, and Z. Liu, *ACS Nano* **5**, 4023 (2011).
- R. H. Baughman, A. A. Zakhidov, and W. A. d. Heer, *Science* **297**, 787 (2002).
- L. Wang, M. Yin, J. Jaroszynski, J.-H. Park, G. Mbamalu, and T. Datta, *Appl. Phys. Lett.* **109**, 123104 (2016).
- J. Jobst, D. Waldmann, F. Speck, R. Hirner, D. K. Maude, T. Seyller, and H. B. Weber, *Phys. Rev. B* **81**, 195434 (2010).

- <sup>10</sup>A. M. R. Baker, J. A. Alexander-Webber, T. Althebaeumer, S. D. McMullan, T. J. B. M. Janssen, A. Tzalenchuk, S. Lara-Avila, S. Kubatkin, R. Yakimova, C.-T. Lin, L.-J. Li, and R. J. Nicholas, *Phys. Rev. B* **87**, 045414 (2013).
- <sup>11</sup>F. V. Tikhonenko, A. A. Kozikov, A. K. Savchenko, and R. V. Gorbachev, *Phys. Rev. Lett.* **103**, 226801 (2009).
- <sup>12</sup>F. V. Tikhonenko, D. W. Horsell, R. V. Gorbachev, and A. K. Savchenko, *Phys. Rev. Lett.* **100**, 056802 (2008).
- <sup>13</sup>S. V. Morozov, K. S. Novoselov, M. I. Katsnelson, F. Schedin, L. A. Ponomarenko, D. Jiang, and A. K. Geim, *Phys. Rev. Lett.* **97**, 016801 (2006).
- <sup>14</sup>E. McCann, K. Kechedzhi, V. I. Fal'ko, H. Suzuura, T. Ando, and B. L. Altshuler, *Phys. Rev. Lett.* **97**, 146805 (2006).
- <sup>15</sup>R. V. Gorbachev, F. V. Tikhonenko, A. S. Mayorov, D. W. Horsell, and A. K. Savchenko, *Phys. Rev. Lett.* **98**, 176805 (2007).
- <sup>16</sup>T. G. Pedersen, C. Flindt, J. Pedersen, N. A. Mortensen, A.-P. Jauho, and K. Pedersen, *Phys. Rev. Lett.* **100**, 136804 (2008).
- <sup>17</sup>J. Eroms and D. Weiss, *New J. Phys.* **11**, 095021 (2009).
- <sup>18</sup>Z. Fan, A. Uppstu, and A. Harju, *Phys. Rev. B* **91**, 125434 (2015).
- <sup>19</sup>T. Khodkov, I. Khrapach, M. F. Craciun, and S. Russo, *Nano Lett.* **15**, 4429 (2015).
- <sup>20</sup>M. Kim, N. S. Safron, M. S. A. Eungnak Han, and P. Gopalan, *Nano Lett.* **10**, 1125 (2010).
- <sup>21</sup>S. Yuan, R. Roldan, A.-P. Jauho, and M. I. Katsnelson, *Phys. Rev. B* **87**, 085430 (2013).
- <sup>22</sup>G. Liu, Y. Wu, Y.-M. Lin, D. B. Farmer, J. A. Ott, J. Bruley, A. Grill, P. Avouris, D. Pfeiffer, A. A. Balandin, and C. Dimitrakopoulos, *ACS Nano* **6**, 6786 (2012).
- <sup>23</sup>X. Miao, S. Tongay, and A. F. Hebard, *J. Phys. Condens. Matter* **24**, 475304 (2012).
- <sup>24</sup>R. Wang, S. Wang, D. Zhang, Z. Li, Y. Fang, and X. Qiu, *ACS Nano* **5**, 408 (2011).
- <sup>25</sup>A. C. Ferrari, J. C. Meyer, V. Scardaci, C. Casiraghi, M. Lazzeri, F. Mauri, S. Piscanec, D. Jiang, K. S. Novoselov, S. Roth, and A. K. Geim, *Phys. Rev. Lett.* **97**, 187401 (2006).
- <sup>26</sup>M. S. Dresselhaus, A. Jorio, M. Hofmann, G. Dresselhaus, and R. Saito, *Nano Lett.* **10**, 751 (2010).
- <sup>27</sup>L. Wang, M. Yin, A. Khan, S. Muhtadi, F. Asif, E. S. Choi, and T. Datta, *Phys. Rev. Appl.* **9**, 024006 (2018).
- <sup>28</sup>B. R. Matis, F. A. Bulat, A. L. Friedman, B. H. Houston, and J. W. Baldwin, *Phys. Rev. B* **85**, 195437 (2012).
- <sup>29</sup>D.-K. Ki, D. Jeong, J.-H. Choi, H.-J. Lee, and K.-S. Park, *Phys. Rev. B* **78**, 125409 (2008).
- <sup>30</sup>X. Hong, K. Zou, B. Wang, S.-H. Cheng, and J. Zhu, *Phys. Rev. Lett.* **108**, 226602 (2012).
- <sup>31</sup>J. Li, L. Lin, D. Rui, Q. Li, J. Zhang, N. Kang, Y. Zhang, H. Peng, Z. Liu, and H. Q. Xu, *ACS Nano* **11**, 4641 (2017).
- <sup>32</sup>H.-C. Wu, M. Abid, Y.-C. Wu, C. Ó. Coileáin, A. Syrlybekov, J. F. Han, C. L. Heng, H. Liu, M. Abid, and I. Shvets, *ACS Nano* **9**, 7207 (2015).
- <sup>33</sup>L. P. He, X. C. Hong, J. K. Dong, J. Pan, Z. Zhang, J. Zhang, and S. Y. Li, *Phys. Rev. Lett.* **113**, 246402 (2014).
- <sup>34</sup>C. Berger, Z. Song, X. Li, X. Wu, N. Brown, C. Naud, D. Mayou, T. Li, J. Hass, A. N. Marchenkov, E. H. Conrad, P. N. First, and W. A. d. Heer, *Science* **312**, 1191 (2006).
- <sup>35</sup>K. Zou, X. Hong, and J. Zhu, *Phys. Rev. B* **84**, 085408 (2011).
- <sup>36</sup>A. H. CastroNeto, F. Guinea, N. M. R. Peres, K. S. Novoselov, and A. K. Geim, *Rev. Mod. Phys.* **81**, 109 (2009).
- <sup>37</sup>J. Bai, X. Zhong, S. Jiang, Y. Huang, and X. Duan, *Nat. Nanotechnol.* **5**, 190 (2010).
- <sup>38</sup>B. S. Jessen, L. Gammelgaard, M. R. Thomsen, D. M. A. Mackenzie, J. D. Thomsen, J. M. Caridad, E. Duegaard, K. Watanabe, T. Taniguchi, T. J. Booth, T. G. Pedersen, A.-P. Jauho, and P. Boggild, *Nat. Nanotechnol.* **14**, 340 (2019).